Analysis & Sensing

Review
doi.org/10.1002/anse.202200005

Chemistry Europe
European Chemical
Societies Publishing

www.analysis-sensing.org

Very Important Paper

Gold Nanostars: Synthesis, Optical and SERS Analytical Properties

I. Brian Becerril-Castro,[a] Irene Calderon,[a] Nicolas Pazos-Perez,[a] Luca Guerrini,[a]
Florian Schulz,[b] Neus Feliu,[b, c] Indranath Chakraborty,[d] Vincenzo Giannini,*[e, f, g]
Wolfgang J. Parak,*[b] and Ramon A. Alvarez-Puebla*[a, h]

Gold nanostars are among the most efficient plasmonic nanomaterials for optical sensing with surface enhanced Raman scattering. In recent years, gold nanostars have increased relevance in physics, analytical chemistry, environmental science, biology and medicine, and in particular in sensing and therapy. These colloids can sustain ultrastrong electromagnetic fields which allow their use as single particles optical enhancers; are colloidally stable and may have a marked catalytical activity. Due to their exotic shape, these colloids present characteristic optical and reactive behaviors. Here, we briefly discuss the optical properties, the synthetic routes and the analytical applications of these nanoparticles.

1. Introduction

Surface-enhanced Raman scattering (SERS) spectroscopy[1] is an ultrasensitive technique which relies on the Raman scattering spectroscopy of the analyte(s) under study on a plasmonic structure, responsible for the generation of the strong electromagnetic field necessary for the signal intensity amplification.

Plasmonic colloids are unique nanostructures capable of exhibiting large electromagnetic fields (i.e., localized surface plasmon resonances, LSPRs) at their surface upon excitation with light of the appropriate wavelength.[2] Besides the composition of the colloidal nanoparticles, the wavelength and intensity of these fields are dependent mainly of three factors: size, plasmon intercoupling between neighbour particles, and shape. Size can be easily tuned for almost any gold shape. However, the impact of the size on the wavelength and intensity of the LSPR is moderate as compared with the other two factors.[3] Particle plasmonic intercoupling notably modifies both, wavelength and intensity of the LSPR.[4] For example, while the LSPR maximum of spherical gold colloids from 10 to 100 nm red-shifts from 520 to 570 nm, the LSPR maximum of an aggregate of 10 nm gold colloids can reach the infrared region. Conversely, the maximum values for SERS electromagnetic enhancement for isolated spherical nanoparticles are on the order of 10^6, while with an aggregate of the same particles that enhancement can go over 10^{10}.[1a] The electromagnetic fields produced by the interaction of different particles is not trivial and, many times, not reproducible from point to point within the same sample,[5] with the subsequent implications in the analytical SERS ultrasensitive detection. Aggregates are also a drawback in some bioapplications, such as intracellular imaging, as for example upon endocytosis of particles by cells modifications in the state of aggregation may occur, making such system vulnerable to signal variations. Finally, the shape is by far the most influencing factor for the LSPR in terms of both, wavelength and intensity.[4] For example, by just modifying the aspect ratio of a rod-shaped nanoparticle, it is possible shifting the LSPR from the red to the infrared.[6]

Tipped nanoparticles such as cubes, rods, or plates show an uneven distribution of the LSPRs over their surface, enabling concentration of light in certain regions which generally match the tips in their structure.[4] However, among these particles, star-shaped colloids (i.e., nanostars, NSts) shine due to their unique optical and colloidal properties. Here, we review such optical properties together with the different procedures to synthesize plasmonic nanostars with tunable characteristics, and their analytical applications.

2. Optical Properties

Light interaction with metal nanostars is extremely intriguing due to the strong extinction cross-section of such structures.[4] Large extinction cross-sections mean that even a few dispersed nanostars interact efficiently with light. Nanostars will also concentrate electromagnetic fields in small regions (hot spots), thanks to the excitation of surface plasmons.[7] Plasmonic nanostars are commonly constituted by a solid plasmonic body, either a sphere, rod, or of other shape, which supports protuberant plasmonic tips. While the body is important, as it supplies electrons to the tips and thus increases the intensity of the electric field as it grows,[8] the main plasmonic features of these structures arise from the tips.[4,9]

Figure 1 shows Boundary Element Method calculations[10] using the MNPBEM toolbox[11] with the dielectric constants from Palik's[12] for gold nanostars consisting of a 40 nm sphere protruded by six tips of different lengths and angles embedded in water (n = 1.33). Every star was modelled using between 3000 and 3100 faces. Electric near-field intensity maps were calculated upon excitation at 785 nm. For the same core, the

---

[a] *I. B. Becerril-Castro, I. Calderon, Dr. N. Pazos-Perez, Dr. L. Guerrini, Prof. Dr. R. A. Alvarez-Puebla*
Department of Inorganic and Physical Chemistry, Universitat Rovira i Virgili, C/Marcel·lí Domingo s/n, 43007 Tarragona (Spain)
E-mail: ramon.alvarez@urv.cat
[b] *Dr. F. Schulz, Dr. N. Feliu, Prof. Dr. W. J. Parak*
CHyN, Universität Hamburg, Luruper Chausse 149, 22761 Hamburg (Germany)
E-mail: wolfgang.parak@uni-hamburg.de
[c] *Dr. N. Feliu*
CAN, Fraunhofer Institute for Applied Polymer Research IAP, Grindelallee 117, 20146 Hamburg (Germany)
[d] *Dr. I. Chakraborty*
School of Basic Sciences, Indian Institute of Technology Mandi, Mandi 175005 (India)
[e] *Dr. V. Giannini*
Instituto de Estructura de la Materia (IEM), Consejo Superior de Investigaciones Científicas (CSIC), Serrano 121, 28006 Madrid (Spain)
E-mail: v.giannini@csic.es
[f] *Dr. V. Giannini*
Technology Innovation Institute, Masdar City, Abu Dhabi, (United Arab Emirates)
[g] *Dr. V. Giannini*
Centre of Excellence ENSEMBLE3 sp. z o.o., Wolczynska 133, Warsaw, 01-919 (Poland)
[h] *Prof. Dr. R. A. Alvarez-Puebla*
ICREA, Passeig Lluis Companys 23, 08010 Barcelona (Spain)

increase of the tip length increases the electric field of the main resonance (dipolar), while slightly shifts the plasmon to the red (Figures 1 A and B). The decrease of the half angle, however, slightly decreases the electric field at the apex of the tip, but dramatically increases the redshift of the dipolar plasmon (Figures 1 C and D). These two parameters can be used to tune the plasmonic response to the appropriate working wavelength.

In contrast with other plasmonic substrates, nanostars decrease their optical efficiency for SERS when they are aggregated.[13] During many years this effect was ascribed to the loss of symmetry between the different nanostars. However, nowadays it is clear that that the interaction of nanostars promotes the formation of hot spots, no matter the geometry of such interaction (Figure 1E). Notwithstanding, such interaction markedly shifts the plasmon towards the infrared (Fig-

I. Brian Becerril Castro received his B.S. degree in Nanotechnology from the Universidad Nacional Autónoma de México (México) in 2017. He is currently a PhD student under the supervision of Prof. Ramon Alvarez-Puebla and Prof. Vincenzo Giannini at the Universitat Rovira i Virgili (Spain).

Neus Feliu is group leader at Fraunhofer Institute for Applied Polymer Research IAP-CAN. She has studied Chemistry at the University of Barcelona and the Royal Institute of Technology, Stockholm, and has obtained her PhD in Medical Sciences at the Karolinska Institutet. She has been postdoctoral researcher at the Karolinska Institutet and the Universität Hamburg, before joining Fraunhofer IAP-CAN.

Irene Calderón obtained her B.S. degree in Human Biology in 2018 at the Pompeu Fabra University (Spain), where she also worked at the Single Cell Behaviour Laboratory. Presently, she is a current PhD student in the Universitat Rovira i Virgili (Spain) under the supervision of Prof. Ramon Alvarez-Puebla.

Indranath Chakraborty is currently an assistant professor at the IIT Mandi. He has obtained his Ph.D. in chemistry from the IIT Madras. He carried out postdoctoral research at the UIUC, USA. Later, he was a Humboldt Fellow at the Philipps University of Marburg. He was also a research associate at the CHyN, University of Hamburg. His research area primarily focused on synthesizing atomically precise nanoclusters and emerging properties of these materials.

Nicolas Pazos-Perez received his PhD in 2008 from the Universidade de Vigo (Spain). He was a post-doc at the Universität Bayreuth (Germany), a Marie Curie IF fellow and a “Ramon y Cajal” researcher at the Universitat Rovira i Virgili. He has been recently awarded with an associate professorship position at the Universitat Rovira i Virgili.

Vincenzo Giannini is a Tenure Scientist at the CSIC, Spain) and the Director of the Metamaterial and Energy Storage division at the TII in Abu Dhabi. He holds a BSC in Physics from the University of Pisa and a PhD from the CSIC and Universidad Autónoma de Madrid. He carried out posdoctoral research at the AMOLF in Amsterdam and was a Marie Curie fellow at the Imperial College London. In June 2014, He started his group at the Imperial College London.

Luca Guerrini received his PhD in 2009 from the Universidad Autónoma de Madrid (Spain) for his work at the Spanish National Research Council. His research experience continued as a post-doc at the Strathclyde University (UK) and, among others, as a Marie Curie IF fellow at the Universitat Rovira i Virgili, where he currently holds a “Ramon y Cajal” grant.

Wolgang J. Parak is Professor at the University of Hamburg. He has studied physics and obtained his PhD in Munich. After a postdoctoral fellowship at Berkeley he returned 2003 to Munich to start his own group. Before moving to the University of Hamburg in 2017 he spent 10 years as professor at the Philipps University Marburg.

Florian Schulz is a senior scientist at the Institute of Nanostructure and Solid State Physics of the University of Hamburg. He obtained his PhD in 2014 in the group of Prof. Horst Weller, followed by a PostDoc in the group of Prof. Holger Lange.

Ramon A. Alvarez-Puebla is an ICREA Professor at the Universitat Rovira i Virgili in Tarragona. He holds a BSc in Chemistry (Universidad de Navarra, 2000) and a PhD in Surface Science (Universidad Publica de Navarara, 2003). He was postdoc at University of Windsor (Windsor, ON, Canada) and General Motors Corporation (Warren, MI, USA) and worked as Research Officer at the National Institute for Nanotechnology of the National Research Council of Canada (Edmonton, AB, Canada) and as Associate Professor at the Universidade de Vigo.

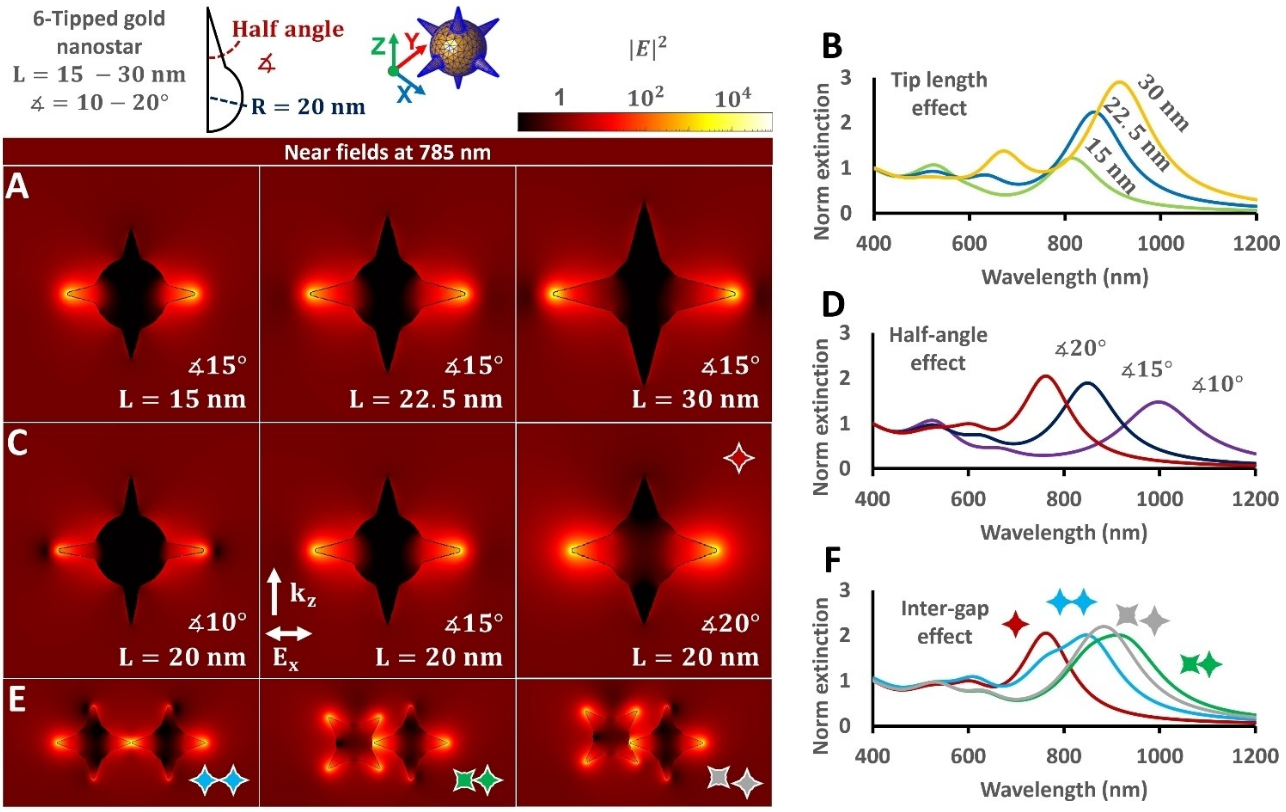

Figure 1. BEM calculations of the near (excited at 785 nm) and far fields for a nanostar composed of a solid spherical body of 40 nm of diameter with six tips as a function of the (A and B) diameter, (C and D) tip half-angle and (E and F) geometry of interaction with another nanostar. Simulations were performed using the MNPBEM toolbox. Every star was modelled using between 3000 and 3100 faces.

ure 1F). As a consequence, conventional Raman systems equipped with laser lines from the blue to the near infrared are unable to overlap with such hotspot, therefore loosing signal intensity.

Finally, although the main optical application of nanostars is in the near infrared region, the excitation with light of shorter wavelength, especially in the blue and green, can excite other hot spots located at the valley between the tips.[14]

3. Synthesis of Au nanostars

3.1. Importance of the seeds

There are many synthetic protocols in the literature to produce branched Au NPs, which can be, nonetheless, broadly classified into two main groups: seedless and seed-mediated methods. Seedless approaches allow for synthesizing Au nanostars in one-pot syntheses, which are usually fast, simple, and often provide high yield. Yet, since nucleation and growth generally occur at the same time, significant polydispersities in size and shape are commonly observed. Differently, seed-mediated approaches allow a temporal separation between these two steps because seed NPs are prepared separately and then subsequently added to a growth solution, where they provide nucleation points for the preferential deposition of additional Au° atoms. Such a two-stage strategy, therefore, allows for a better control over shape and size.[15]

The characteristic of seeds is of crucial importance in terms of crystallinity and size of the resulting branched nanostructures. In fact, the different surface energies of the crystal facets of the seeds and the affinity to the capping agents drive the selective deposition of gold atoms defining the final morphology of the NPs. In general, the presence of (111) twin planes on the seeds is necessary to growth branched structures. The most commonly employed seeds are polycrystalline (multitwinned) gold NPs.[16] However, it has been also proposed that single crystalline seeds can be used for the growth of branched nanoparticles by controlling the growth of the seeds into NPs with twin planes.[17] In addition to gold, other noble metals have been also utilized as seeds to grow Au NSts. For instance, small single crystalline platinum seeds have been used to produce small and well-defined nanostars.[18] In this case, the authors also reported the development of twin planes during the growth process but to a smaller extent, producing, therefore, a lesser number of branches. As expected, the size of the seeds itself plays an important role in defining the final nanostar features as the number of surface defects increases with the size.[19] In particular, it has been reported that for Au NSts the size of the seeds influences mainly the final NSts dimensions, but does not lead to major differences in the optical properties of the tips. Nonetheless, when smaller seeds were used, fewer spikes were observed, leading to narrower plasmon bands,[18] and an increase in the relative length of the branches due to the smaller cores.[18–19,24] All these effects are in agreement with the smaller number of surface defects for small seeds.

Another important aspect in the seed-mediated methods is the timing of their addition to the growth solution. If the seeds are added in the presence of Au(III), an increase in NSt polydispersity occurs due to partial oxidation of the seeds. On the contrary, a delay in the addition of the seeds can induce nucleation, since the growth solutions reduce Au(I) into Au(0), Therefore, the optimum time to combine seeds and growth solution is when the gold precursor is fully reduced to Au(I).[18]

Finally, the ratio of the seeds vs the Au precursor is also critical in the NSt preparation. It has been observed that, as the number of seeds increases relatively to Au(III) content, less gold is available which, in turn, reduces the branch density causing a blue-shift and narrowing of the plasmon resonances.[18,25]

3.2. Asymmetric multi-spiked nanostars

The first and most widely used method for synthesizing Au NSts consists of a seed-mediated approach that involves the reduction of gold ions driven by polyvinylpyrrolidone (PVP) in dimethylformamide (DMF), where PVP also acts as a stabilizing agent. In general, the syntheses consist of the addition of preformed PVP-stabilized gold seeds in ethanol to a growth solution comprising PVP, DMF, and a gold salt (i.e., $HAuCl_4$). A key feature of this method is the large PVP/Au molar ratio, which enables the reproducible production of Au nanostructures in high yields.[20] However, the PVP concentration and molecular weight are additional parameters to take into account since the reducing power of PVP affects the kinetics of the anisotropic growth of Au NSts. High molecular weight PVP imparts better NPs stabilization due to a higher steric hindrance but, on the other hand, determines a higher reducing power because of the larger number of reducing active sites. Therefore, the faster is the reduction of Au^+ to Au^0, the lower is the extent of the anisotropic growth.[26] This synthetic route allows for controlling the final size of the stars by varying the concentration of Au seeds added to the growth solution from approximately 45 to 116 nm, thus allowing the fine-tuning of the LSPR in the 725–850 nm range (Figure 2A).[21]

Such PVP seed-mediated synthesis was also used to grow tips onto non-spherical structures like thorned rods and wires,[22] as shown by Aldeanueva-Potel et al.[8] who fabricated a new family of spiked particles using penta-twinned gold nanorods as seeds. The authors showed that low $[HAuCl_4]$/[Au seed] ratios lead to a roughened morphology with slight transversal growth of the initial rods, while for higher ratios the thorned structures became wider, converting the final particles into a sort of spiked beads (Figure 2B). Such geometrical reshaping is directly reflected in the SERS enhancing performances of the substrates, with an increase in signal intensity observed for a higher number of spikes and larger spike sizes. The SERS response of the spiked beads has been also tested upon assembling the particles in a thin film. Low-density particle film yields SERS signal comparable to the one acquired from the colloidal suspension. On the other hand, a drop in the optical signal is detected for high-density particle films due to tip-to-tip interactions.[8]

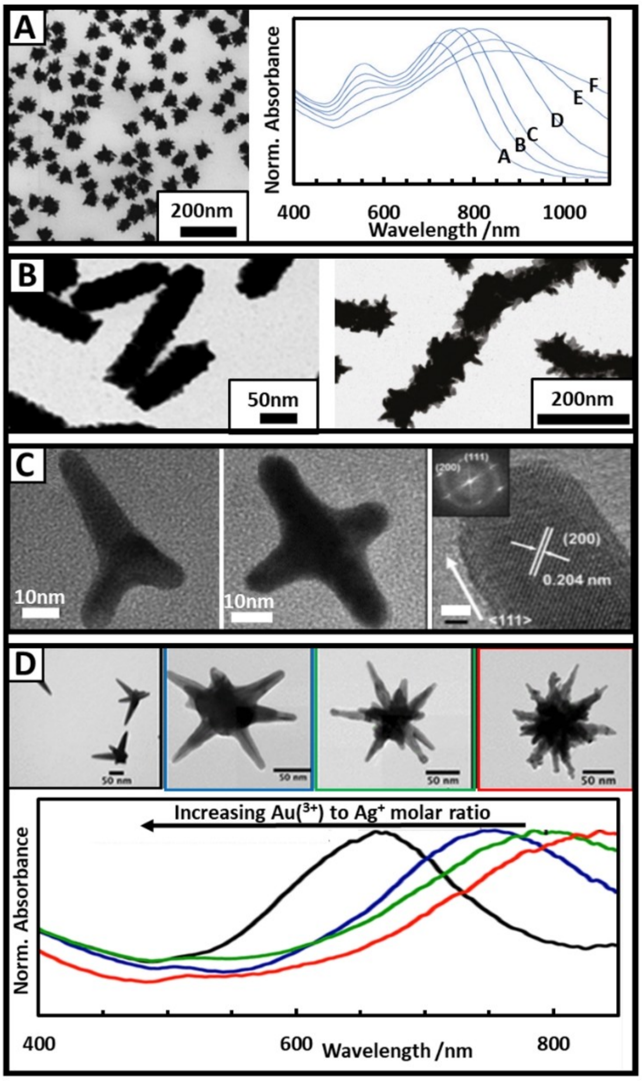

Figure 2. (A) Left: TEM image of Au NSts synthesized in PVP/DMF. Right: Extinction spectra of nanostars of increasing size (from A to F are: 45, 52, 57, 72, 94, 116 nm) synthesized with PVP. (B) TEM images of particles resulting from growing NSts using gold nanorods (left) and nanowires (right) as seeds. (C) Representation of the different morphologies observed in a synthesis of NSts using HEPES. A HRTEM image of one tip, where the (111) growth direction is shown, is also included. (D) Influence of the Au(III) to Ag(I) molar ratio in the of NSts synthesis using ascorbic acid (AA). TEM pictures and their respective extinction spectra. Red corresponds to a ratio of 8.2, green to a ratio of 12.3, blue to a ratio of 49, and black to a ratio of 100. Scales bars are equals to 50 nm. (A) Left: Adapted with permission from ref [20]. Copyright 2008, IOP Publishing. Right: Adapted with permission from ref [21]. Copyright 2008, American Chemical Society. (B) Left: Adapted with permission from ref [8]. Copyright 2012, John Wiley & Sons, Inc. Right: Adapted with permission from ref [22]. Copyright 2010, American chemical Society. (C) Adapted with permission from ref [23]. Copyright 2015, Royal Society of Chemistry. (D) Adapted with permission from ref [24]. Copyright 2018, American chemical Society.

It is worth noting that, despite being the PVP-based synthesis an established protocol in materials science, fundamental research interest is still ongoing with several studies aiming for an improved mechanistic understanding and elucidation of the complex interplay of different parameters including the role of precursor complexes and the pH.[27] Emerging techniques as liquid-cell in situ TEM can provide valuable insights in this respect.[28]

Such synthetic route also displays important disadvantages in the integration of NSts into optical sensors. On the one hand, PVP-coating of the nanoparticle requires tedious cleaning procedures to grant molecules accessibility to the plasmonic surface. On the other hand, the generated NSts are stable in DMF or ethanol and, thus, has to be further transferred to water to be used in biological systems. To this end, new synthetic strategies have been pursued to produce spiked NPs in aqueous media and improve their biocompatibility. For instance, glucosamine has been employed as a biocompatible stabilizer and anisotropic directing agent in an eco-friendly approach. This method yields multibranched colloids with an inner core of 28±5 nm and a total size-tuneable from 55 to 72 nm by using different [glucosamine]/[$HAuCl_4$] ratios.[29]

The direct synthesis of aqueous biocompatible NSts has been also carried out using 2-[4-(2-hydroxyethyl)-1-piperazinyl]-ethane sulfonic acid (HEPES) as a caping and shape-directing agent (while the piperazine moiety is responsible for producing nitrogen-centered free radicals, which can reduce Au(III)).[30] HEPES-based strategies allow the generation of 60 nm sized branched colloids at room temperature (RT) with a one-pot, fast and simple route.[31] The intrinsic limitation of the seedless approach at controlling the branch formation and NSt homogeneity has been partially tackled by varying [$HAuCl_4$]/[HEPES] ratio and reaction temperature.

A temperature increase reduces the tips length until only spheres were obtained at boiling temperature, while working in an ice bath favours the growth of symmetric face-centered cubic (fcc) facets. A relative increase in the precursor salt concentration results in branches with a higher aspect ratio, while the plasmonic feature broadens and red-shifts.[29–30,32] HRTEM images reveal that the growth direction of the tips is along the [111] direction as shown in Figure 2C. In any case, although the tips are homogeneous with a narrow plasmonic response, they are not very sharp and the synthesis results in a non-homogeneous mixture of NSts with a different number of branches (Figure 2C). Within the context of SERS applications, however, the HEPES-based method does offer the advantage of easy removal of the surfactant from the gold surface.[33] Although they are not as versatile as HEPES-based strategies, other analogous surfactant-free methods employing 4-(2-Hydroxyethyl)-1-piperazinepropanesulfonic acid (EPPS) and 3-(N-morpholino)propane sulfonic acid (MOPS) were also developed.[23,34]

Alternatively, proteins can also be used as shape-directing and stabilizing agents. Proteins have two advantages over other shape-controlling surfactant molecules, since the resultant particles will have better biocompatibility and less protein corona formation. Although many proteins can be used to synthesize these NSts, the best quality NSts (homogeneity) could be obtained by using bovine serum albumin (BSA).[35] The synthesis of BSA-coated AuNSts involved a two-step seed-mediated route. First, the Au seeds were prepared at high temperature (~90 °C) in an aqueous medium. The seed solution must be stored in the fridge (4 °C) for 24 h before use. Then in the second step, NSts were grown in the presence of BSA and ascorbic acid as a mild reducing agent. The resultant blue colored AuNSts show a broad absorption peak centered around 590 nm with an average core diameter and tip length of 70±5 nm and 12±5 nm respectively.[35]

Besides the goal of improving biocompatibility, great efforts have been devoted to achieving more defined and homogeneous structures with a precise number of tips. In this regard, since cetyltrimethylammonium bromide (CTAB) has been commonly used to induce anisotropic growth in nanorod synthesis, it has been proposed as an alternative to PVP in NSt seed-mediated protocols. In this case, the preferential capping of CTAB to specific crystallographic planes of the seeds, induces the growth of asymmetric fcc lattices.[36] Moreover, the use of ascorbic acid (AA) as a reducing agent in combination with $AgNO_3$ as a co-direct agent promotes the blocking of specific crystallographic planes, allowing for the reduction of Au(III) in the appropriated sites. This yielded nanoparticles with well-defined tips, but with poor control over the number of tips per particle (from 1 to 6), probably due to the different crystallographic defects present on the small Au seeds.[36] An analogous approach but using Ag plates as seeds has lead to the production of monopods, bipods, tripods, and tetrapods combined in a pool of diverse morphologies as similarly observed for HEPES (Figure 2C).[37] SERS characterization studies of these nanoparticles revealed enhancement factors around 4×10^5.[38] CTAB-based seedless strategies were also pursued, demonstrating their ability to generate NSts in a very simple fashion but, again, leading to polydispersed multi spiked geometries.[39] Notably, replacing CTAB with benzylhexadecyldimethylammonium chloride (BDAC) in combination with anionic dioctyl sodium sulfosuccinate (AOT) and sodium dodecyl sulphate (SDS), allowed the acquisition of well-defined multibranched Au NSts with LSPR tuned from 550 nm to 1100 nm ($AgNO_3$ and AA were maintained in the synthesis as direct and reducing agents, respectively).[40] The size of the cores and the whole NSts increased with BDAC concentration. SERS enhancement factors (EFs) were estimated to be about 1.5×10^4.[40] The role of BDAC was found to lower the critical micelle concentration (CMC), and replace the bromide ions with chloride, favoring the formation of sharp tips because it facilitates the adsorption of silver ions onto the surface of the growing Au seeds.[41]

The use of lauryl sulfobetaine (LSB) as a shape directing zwitterionic surfactant has also proven to help to restrict the uncontrolled formation of a different number of spikes. Using a seed-mediated approach, monocrystalline Au NSts and penta-twinned gold asymmetric NSts were fabricated. The growth process implies preferential coating of the {111} Au faces through weak binding of sulphate moiety of LSB.[42] By adjusting the AA, LSB, and Ag^+ concentrations in the growth solution, it was possible to control the branches aspect ratio and, consequently, finely tuning the LSPR in the 750–1150 nm range.[42]

A surfactant-free, seedless method has been developed using hydroquinone (HQ). HQ is a water-soluble, weak reducing agent that favors gold deposition on the [111] facet. The main advantages of this method are simplicity and quickness. However, particles are not colloidally stable for more than a few hours, unless sodium citrate is added to the mixture, and display short branches with tips of reduced sharpness. This is also reflected by the relatively low SERS enhancing performances (EF $\sim 3\times10^3$)[43] and a LSPR positioned around 620 nm. When the co-reduction agent sodium citrate is added separately from hydroquinone during the synthesis, improved control over the branch morphology is achieved.[44] When the HQ approach is integrated into seed-mediated methods, NSt monodispersity and geometrical tunability improve, enabling the control of particle size from 55 to 200 nm (LSPR from 555 to 702 nm).[45] Additionally, the inclusion of starch as an additive boosts the colloidal stability up to a month. Nonetheless, the SERS EF remains mostly unaltered.[46]

As a non-ionic surfactant, Triton X-100 assists the formation of NSts in aqueous media acting, first, as micellar templates with a hexagonal phase and, second, as a stabilizer preventing aggregation for several months. In the presence of AA as a mild reducing agent and $AgNO_3$ as a directing agent, well-defined NSts with long, twinned thorns are obtained. By simply varying the amount of the silver additive, it is possible to synthesize NSts with very different size and morphology, even with tips longer than 100 nm. Another important variable in this synthesis is the temperature. NSts produced in ice-cold conditions develop longer tips, meanwhile increasing the temperature up to 36 °C induces the formation of short spikes.[47] Their plasmon resonance shows a broad absorption peak from 600 to 900 nm.[47b] Notably, since Triton X-100 has a weak affinity for gold, it allows an easy functionalization of these structures.[17a,48]

Surfactant-free approaches using citrate and ascorbic acid as stabilizers, and reducing agents provide biocompatible nanoparticles and ease their surface post-modification for SERS applications. In these synthetic methods, the addition of Ag^+ is central to break the symmetry of the seeds during the growth process[49] and, thus, the resulting NSts are very sensitive to the ratio between the two metal precursors (Figure 2D). Typically, higher amounts of Ag give rise to more tips per particle but with shorter geometry, while lowering the silver content induces lesser and longer tips.[24] Likewise, it has been shown that when using citrate stabilized Au NP seeds of different sizes in the presence of $HAuCl_4$, $AgNO_3$, HCl and AA, branched NPs with average sizes ranging from 45 nm to 150 nm can be prepared. The corresponding plasmon resonances are between 630 nm to 900 nm.[24,50] These studies conclude that as the seed size increases, smaller cores and tip-to-tip diameters are created, while with smaller seeds facilitate the formation of longer branches. They also observed the possibility to adjust the LSPR peak position by controlling the seed concentration or by tuning the chemical affinities of Au-halide that promotes changes on the shape evolution of the branched nanoparticles. By systematically studying synthesis parameters like stirring speed, pH, reagent and additive concentrations, it was possible to optimize the two photon absorption cross-section of the NSts for a given NIR laser excitation.[51] In a follow-up study, the multiplexing capability of the NSts was also proven, underlining their potential for biomedical imaging.[52] A table summarizing the roles of the most common reagents used to produce Au NSts is shown in Table 1.

In addition to the aforementioned synthetic protocols, the use of microfluidic technology has been also implemented in the past years in nanofabrication methods to improve the reproducibility of monodisperse branched gold nanoparticles. In fact, this technique enables precise control over the reagents mixing rate, volumes, and temperature thereby offering a valuable tool for reproducible and continuous fabrication of nanoparticles. In this context, two main approaches, continuous vs droplet flows, have been used for AuNSt synthesis. For instance, using a continuous flow, Au NSts of around 50–70 nm

Table 1. Summary of the specific roles for the most common reagents used in the synthesis of Au NSts including their advantages and disadvantages.

Reagent & Role	Advantages	Disadvantages
PVP[a] Stabilizer Reductor Shape directing	Size control Tunable LSPR Biocompatible	Seeds preparation Surface cleaning Organic media
GS[b] Stabilizer Reductor Shape directing	Aqueous Biocompatible	No size control No tunable LSPR
HEPES[c] Stabilizer Reductor Shape directing	Aqueous Biocompatible	No size control Polydisperse NSTs
BSA[d] Stabilizer Shape directing	Aqueous Biocompatible	Seeds preparation No size control No tunable LSPR
CTAB[e] Stabilizer	Aqueous	Seeds preparation. Polydisperse NSTs. Surface cleaning
CTAB/BDAC[f]**/ AOT**[g]**/SDS**[h] Stabilizer	Aqueous	Seeds preparation No tunable LSPR Surface cleaning
LSB[i] Stabilizer Shape directing	Aqueous Tunable LSPR Long tips	Seeds preparation No tunable LSPR
HQ[j] Reductor	Aqueous	Seeds preparation No colloidal stable No tunable LSPR Short tips
TX-100[k] Stabilizer Shape directing	Aqueous Size control Biocompatible Long tips Easy functionalization	T° control No tunable LSPR
AA[l] Reductor	Aqueous Biocompatible Easy functionalization	Seeds preparation No tunable LSPR Polydisperse NSTs

[a] Polyvinylpyrrolidone. [b] Glucosamine. [c] 2-[4-(2-hydroxyethyl)-1-piperazinyl]-ethane sulfonic acid. [d] Bovine serum albumin. [e] Cetyltrimethylammonium bromide. [f] Benzylhexadecyldimethylammonium chloride. [g] Dioctyl sodium sulfosuccinate. [h] Sodium dodecyl sulphate. [i] Lauryl sulfobetaine. [j] Hydroquinone. [k] Triton X-100. [l] Ascorbic acid.

have been produced in a seedless approach mixing a solution of $HAuCl_4$ and $AgNO_3$ with AA and NaOH.[53] On the other hand, a droplet microfluidics method has been exploited to yield monodisperse Au NSts of 60–80 nm size. In this case, two seed-mediated synthetic approaches were tested: (i) a surfactant-free method in water using $HAuCl_4$, $AgNO_3$, HCl, AA, and the seeds, and (ii) a PVP based approach in DMF using PVP, $HAuCl_4$, and seeds.[54] According to the study, the droplet microfluidic platform provides higher quality Au NSts due to the better mixing of the reagents in the drops.[55]

3.3. Synthesis of symmetric nanostars with a defined number of tips

Conventional approaches for NSt synthesis can afford homogeneous particle sizes, but commonly fail to accurately control the tip growth, which results in the formation of nanostars with a different number of branches of diverse geometries.[4,25] This has a direct impact on the particle-to-particle optical behavior as SERS enhancers which, in turn, restrict their use for quantitative analysis. Thus, great efforts have been devoted to designing structurally alike spiked particles with a uniform optical response.

For instance, a synthetic route using a non-polar solvent has been proposed to avoid electrostatic interactions during the growth process. To this end, toluene was selected as a solvent and oleyl amine (OAm) was used to solubilize $HAuCl_4$ and produce an organo-gold precursor.[59] To induce the formation of branches, copper was used as a templating metal through a galvanic replacement. It was shown that, by appropriately lowering the temperature, the length of the branches increases with the reaction time. Thus, the branch length can be tuned from 50 nm to over 200 nm, resulting in a LSPR progressively red-shifted from 850 nm to 1880 nm.

PVP-based seeded growth synthesis on preformed multibranched NSts has been also reported to improve the control over the nanoparticle morphology. Here, during the overgrowth stage, the branches merged, forming a larger core with a defined number of branches, which became thicker and shorter during the process, paving the way for LSPR tuning in the 570–1100 nm range. SERS enhancement properties of Au NSts with plasmon resonances ranging from 600 to 900 nm were studied using 633 and 785 nm laser lines, indicating a positive correlation between the matching of the laser line wavelength and LSPRs with the SERS intensity.[60]

Alternatively, it has been demonstrated that by carefully controlling the kinetics of the reaction and the crystallinity of the seeds it is possible to synthesize homogenous pentastars with defined optical properties (Figure 3A).[56] In the standard PVP-based method, DMF acts as a solvent and simultaneously increases the PVP solubility, which strengthens the polymer reducing capacity. When replaced by ethanol, the weaker polarity of the solvent makes PVP less soluble which, in turn, slows the reaction rate. This, in combination with well-defined penta-twined seeds, allows growing pentastars with uniform branches. The SERS activity of 50 nm size pentastars (LSPR centered at 695 nm) under a 785 nm laser excitation showed to be larger than spherical and asymmetric multibranched NSts of analogous size, with an estimated EF $\sim 5 \times 10^6$. This has been attributed to the homogeneity of the tips. In another notable example, highly symmetric NSts were obtained by using icosahedral seeds that were overgrown in the presence of PVP and DMF.[57] In this case, dialkylamine was used as an additive to regulate growth by stabilizing high-index facets. The produced NSts exhibit the same icosahedral symmetry as the seeds (Figure 3B) and an extinction spectrum with a strong contribution of the core (below 600 nm).[57] In a similar study, tetrapods of high symmetry were synthesized in DMF and PVP using diethylamine as a capping agent to block the {100} facets

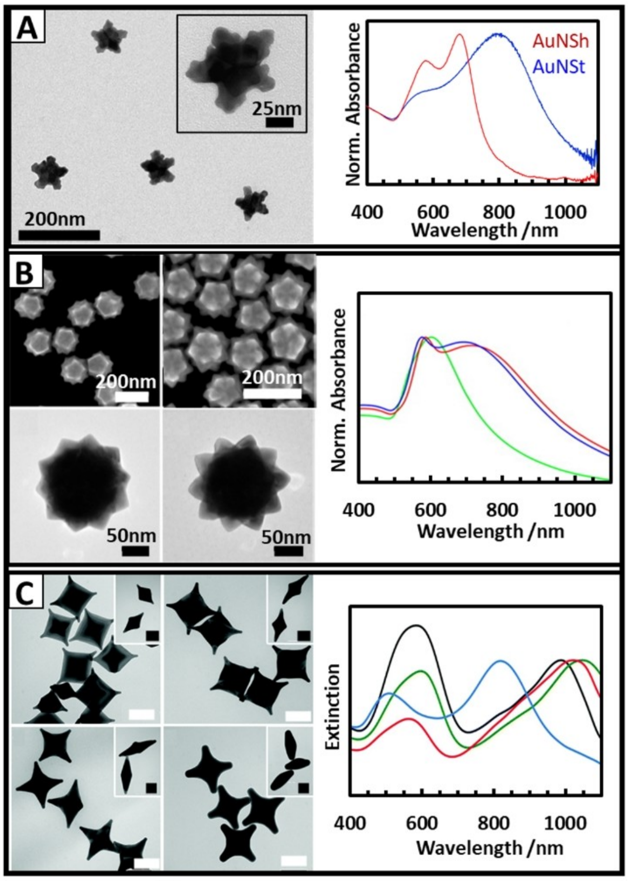

Figure 3. (A) Left: TEM image of Au pentastars (NSh) synthesized using PVP in ethanol. Right: Comparison of the extinction spectra of NSh and regular multibranched NSts. (B) Left: TEM image of highly symmetric Au NSts prepared with the standard PVP-DMF approach but using icosahedral Au NPs as seeds. Right: Extinction spectra of Au nanostars with sharp and round tips (red and blue, respectively); the green curve corresponds to dodecahedral Au nanocrystals used as seeds. (C) Left: TEM images of Au NSts with 4 branches showing tips of different lengths and sharpness obtained at different temperatures (60, 80, 100 and 150 °C) and reaction times (90, 40, 10 and 10 min), respectively. The insets show the nanostars standing on their lateral sides. The scale bars are equals to 100 nm for the images and 50 nm for the insets. Right: Corresponding extinction spectra of the Au nanostars synthesized at different temperatures (black 60 °C, green 80 °C, red 100 °C, and blue 150 °C). (A) Adapted with permission from ref [56]. Copyright 2014 The American Chemical Society. (B) Adapted with permission from ref [57]. Copyright 2015 The American Chemical Society. (C) Adapted with permission from ref [58]. Copyright 2017 The Royal Society of Chemistry.

and, thus, induce the preferential growth in the [110] directions. The morphology of these structures is highly dependent on the reaction temperature. At low temperatures (60–80 °C), the obtained structures have short and sharp tips. At 100 °C, the tips grew much longer and became sharper (see TEM images in Figure 3C). These nanostructures have a LSPR in the NIR range, as seen from Figure 3C. Beyond this temperature, the tips started to blunt, with the corresponding blue-shift of the LSPR.[58]

CTAB-based synthetic routes to produce NSts with a defined number of tips were also investigated. For instance, CTAB was mixed with protoporphyrin IX to form a complex that, in combination with $AgNO_3$, operate as a shape-directing agent, leading to the formation of ca. 50 nm AuNSts with very short and thick apexes. In addition to a broad, red-shifted feature ranging from approx. 550 to 650 nm, the extinction spectrum also shows a contribution at around 400 nm assigned to Ag.[61] Similar results were obtained using a mixture of CTAB and CTAC to control the respective bromide and chloride concentrations. NSts with five symmetrical branches or penta-branched NPs with a pentagonal-bipyramidal shape were obtained. No plasmonic contributions from Ag were distinguished in the extinction spectra.[62]

Deep eutectic solvents (DES) are gaining attention in the production of noble metal nanoparticles because of their low cost, non-toxicity, and biodegradability. Furthermore, thanks to their extensive hydrogen-bond network DES can be used as soft templates for enhancing shape-control of the nanostructures. An illustrative example was reported by Liao et al.[63] Here, DES was prepared by mixing choline chloride and urea, and used to separately dissolve $HAuCl_4$ and AA. The two solutions were then combined and maintained at 30 °C to generate NSts. The overall water content is crucial for the final particle shape. When the water is fully removed, the authors obtained nanoparticles with 5 branches along the (111) facets with the ends of the branches forming a tetragonal micro pyramid (Figure 4A). Conversely, when the water content rises above ca. 5000 ppm, well-defined star-shaped particles were obtained. A large content of water ($>$10000 ppm) leads to the formation of multispiked structures.

A further synthetic approximation to construct symmetric structures relies on the careful control of the reducing agent (AA) concentration in the presence of Triton X-100. High AA contents make the reduction process too fast, which hinders the Triton X-100 preferential adhesion onto the {111} Au facets, thereby yielding disordered multispiked particles (Figure 4B).[64] HRTEM shows that this type of NSts is crystalline, where the growth of the branches takes place along the {111} twinning boundaries of the pentatwinned crystal cores. Moreover, a closer look reveals a pentatwined structure of the tips (Figure 4B). The quality of the NSts can be improved using Ag^+ as an additive. $AgNO_3$ plays a crucial role in determining that the single crystal seeds used become penta-twinned intermediates, which promotes the growth of the branches. Similarly, shape and size of the branches can also be tuned by adjusting the $AgNO_3$ concentration (the branch length increases with the Ag(I) content, Figure 4B). On the other hand, altering the number of seeds impacts the NSts size, which can be reduced as far as 46 nm. Extinction spectra show three LSPRs in the 350–1800 nm range: a very weak one at 530–560 nm (transverse LSPR from the branches), a moderately intense one in the 600–900 nm range (longitudinal LSPR from the single branches), and the most intense in the 1100–1600 nm range (longitudinal LSPR from the aligned spikes within the individual stars). A SERS EF of ca. 7×10^3 has been reported for this class of nanostars.[65]

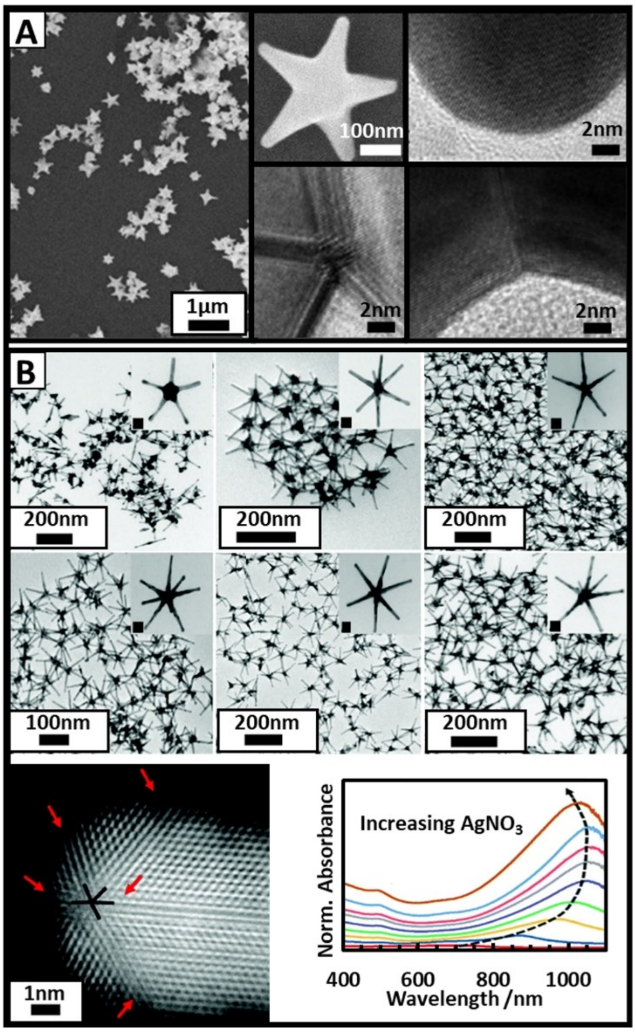

Figure 4. (A) Left: SEM images of Au pentastars with a defined shape synthesized in DES. Right: SEM and HRTEM images showing the crystallinity of the core which shows a clear pentatwined structure with five {111} planes. Each of these planes is the boundary between tips that growth in the (111) direction. (B) Top: TEM images of Au NSts prepared with Triton X-100 as a surfactant and at increasing $AgNO_3$ concentrations (30, 40, 50, 60, 70 and 80 µM). Insets scale bars equals to 20 nm. Bottom left: STEM picture of the tip in which the five twining planes are shown, indicating that the spikes are formed on the twinning axis of a pentagonal unit. Bottom right: extinction spectra for each colloidal dispersions demonstrating a gradual red-shift with increasing $AgNO_3$ concentration (a final blue shift is observed when the silver starts to deposit at the core). (A) Adapted with permission from ref [63]. Copyright 2008, John Wiley & Sons, Inc. (B) Adapted with permission from ref [17a]. Copyright 2019, The Royal Society of Chemistry.

3.4. Hybrid Nanostars

Preventing uncontrolled NSt aggregation is mandatory to avoid tip-to-tip interactions that would dump the SERS enhancing ability of the individual nanoparticles under illumination with conventional lasers.[66] In this regard, NSt colloidal stability is particularly threatened when molecules present in the investigated media displace the stabilizing surfactants from the plasmonic surface.

To tackle this issue, several nanofabrication procedures were implemented to guarantee stability against aggregation while allowing the diffusion of small molecules onto the NSt surface. For instance, polymers like dodecyl amine-modified polyisobutylene-alt-maleic anhydride (PMA) or poly-(N-isopropylacrylamide) (pNIPAM) microgel coatings have been used to covering Au NSts with protective and porous outer layers (Figure 5A).[67] In the case of pNIPAM, besides imparting long-term colloidal stability in complex aqueous solutions, additional functionality is integrated into the hybrid nanoparticle. In fact, pNIPAM shells can swell or collapse as a function of temperature, a phenomenon that can be used to selectively trap molecules close to the metal core for sensing and drug loading.[67b] Although a direct pNIPAM coating of gold NSts is viable,[68] it requires the design of specific chemical routes to develop the structures. As an alternative, coated nanostars can be derived from seeds, coated with the polymer, by using standard NSts synthetic procedures to grow tips on the seeds.[69]

Nevertheless, silica is by far the most widely used material for NPs coatings (Figure 5B) and a plethora of modifications of the well-known Stöber method[70] have been developed for this purpose. Typically, an alkoxy silane is added to an ethanolic solution containing the NPs, while small amounts of water and a base are used to initiate the hydrolysis and silica condensation onto the NPs surface. To achieve a homogeneous coating, NSt surfaces need to be equipped with enough amenable groups for silane condensation. Therefore, molecules like PVP, carboxylic groups, or alcohols have been commonly implemented onto the gold surface via direct surface functionalization or layer-by-layer (LBL) coating.[71] It is worth noting that different Raman active molecules can be also incorporated into the silica matrix during its growth process.[71b] In recent years, metal-organic frameworks (MOFs) are emerging as an intriguing alternative to silica coating because of their unique physicochemical features and tunable porous structure. Zeolitic imidazolate framework (ZIF-8), a relatively hydrothermally stable MOF, is the most common choice for coating gold nanoparticles. Unfortunately, MOF-coating commonly leads to relatively thick shells, like the ones shown in Figure 5C.[7572], while the experimental procedures are more challenging than the silica ones. However, coating gold NSt via direct adhesion with an outer shell passivates the plasmonic surface to a significant extent, thereby restricting the availability for interactions with analytes even for thin mesoporous silica layers.

An intriguing strategy to tackle this problem is designing yolk-shell structures comprising a porous outer shell and a hollow cavity containing the plasmonic particles. In this scenario, the NSts are efficiently protected from unwanted interparticle coupling, while their surface is fully available for chemical modification. Cleaning of spurious surfactants can be performed without endangering the colloidal stability while the porous silica shell also acts as molecular sieving to allow only small molecules to cross through the pores.[76] In order to produce such structures, small spherical NPs are pre-coated with polystyrene (PS) and, subsequently, with mesoporous silica (Figure 5D).[77] PS is then removed either by solvent dissolution or calcination, a process that also leads to a cleaner metallic surface and the hardening of the silica shell, which prevents the dissolution in aqueous media. Finally, the entrapped nanospheres were used as seeds to grow NSts inside the shell.[13] Another example of yolk-shell structures has been

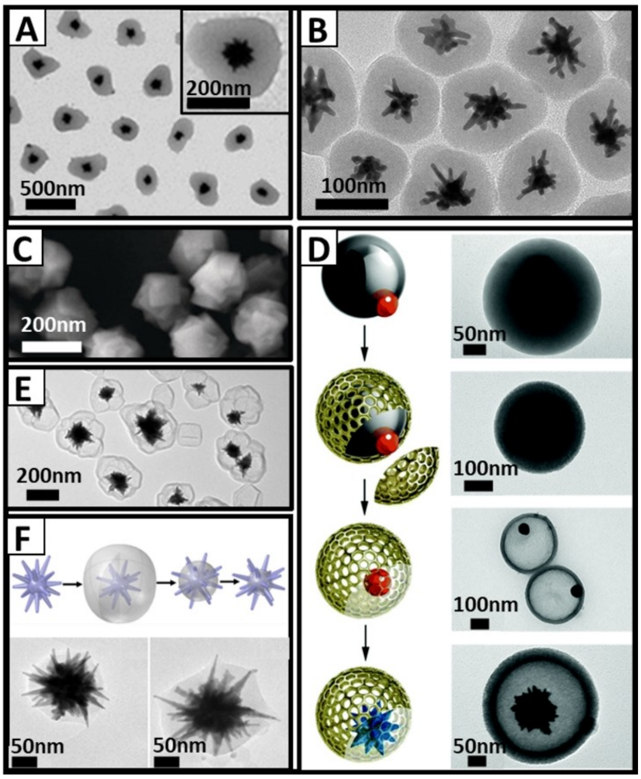

Figure 5. (A) TEM image of gold nanostars coated with pNIPAM. (B) TEM picture of Au NSts coated with silica. (C) SEM image of the nanostars coated with ZIF-8. (D) Scheme of the protocol to produce yolk-shell structures and their respective TEM images. First, nanospheres are added to an emulsion polymerization reactor where single colloid is entrapped in a polystyrene bead. After that, the bead is coated with a mesoporous silica that is later calcined producing the yolk shell structure. Finally, the nanoparticles can be overgrowth into stars inside the structure. (E) TEM image of yolk-shell structure of gold nanostars coated with MOF. (F) Scheme of the structures obtained with the isotropic etching of silica coating to expose only the tips of the nanostars. The scheme is accompanied with TEM pictures of the silica-coated Au NSts at 0 min (left) and 45 min (right) during the etching process observing the decrease of the silica thickness with time. (A) Adapted with permission from ref [68]. Copyright 2012 The Royal Society of Chemistry. (B) Adapted with permission from ref [71b]. Copyright 2011 The American Chemical Society of. (C) Adapted with permission from ref [72]. Copyright 2019 John Wiley & Sons, Inc. (D) Adapted with permission from ref [13]. Copyright 2019 The Royal Society of Chemistry. (E) Adapted with permission from ref [73]. Copyright 2019 The American Chemical Society. (F) Adapted with permission from ref [74]. Copyright 2020 John Wiley & Sons, Inc.

recently reported by Deng et al.[73] who coated AuNSts with Zif-8 and removed the inner layer via selective etching with tannic acid (Figure 5E).

Finally, Fabris and co-workers[74] described an interesting approach to impart colloidal stability while boosting the sensitivity of gold nanostars. In their study, a continuous silica shell is initially grown on the NSt surfaces, followed by its controlled isotropic etching in the presence of sodium borohydride, which leaves the gold structure unaffected. As a result, nanostar spikes, whose tips concentrate the highest electromagnetic enhancements, are selectively exposed from the silica shell to the surrounding media (Figure 5F) without affecting the colloidal stability imparted by the silica coating.

4. Analytical properties of Au NSts

Though the analytical qualities of a SERS method should be ideally designed and assessed according to the requirements of the specific application, there is a general agreement that, while high sensitivities can be consistently achieved, implementation of SERS to robust quantitative analysis has traditionally posed important challenges.[78] Besides the nature of the plasmonic substrates, several other factors have been recognized to play a relevant role in determining the analytical performance of SERS, from the choice of the experimental set-up and protocols for sample preparation to the methods for data analysis.

As mentioned before, AuNSts have been attracting great interest as nanomaterials for SERS applications since they inherently provide very large enhancing capabilities at a single-particle level and, when properly designed and used, can afford quantitative response. For their integration as SERS platforms, a key feature of AuNSts is certainly the extremely high differences in local electric fields at different points of the nanoparticle with large enhancement factors (ca. 10^{10})[79] concentrated at the tips while much lower values (ca. 2–3 orders of magnitude)[66] are observed at the sphere-like core regions for a monolayer coating of Raman labels (RL).[20] Thus, the SERS response is dominated by the relatively small fraction of molecules adsorbed onto the tips, which clearly stress the importance of the efficient localization of the Raman scatterers in these regions. In a seminal study, Rodriguez-Lorenzo et al.[79] organized on top of an optically thick gold substrate a mixed layer consisting of a small fraction of a SERS- active dithiol molecule (1,5-naphthalenedithiol; 1,5-NAT) integrated into a monolayer of 1-octanethiol (1-OT), characterized by a rather poor Raman cross-section. Subsequent addition of NSts (50 nm size, LSPR around 730 nm) promoted the covalent binding of the gold tips to the free thiol group of 1,5-NATs, yielding tip-to-gold film hot spots with a gap distance equals to the length of the dithiol molecule. This method allows the selective localization of the RL at the NSt tip so that each gap will contain only one or a few SERS-active molecules entailing intensification of ca. 10^{10} times. As it is expected, the average signal enhancement decreases when 1,5-NAT molecules are freely distributed over the entire NSt surface, such as when RL is directly combined with the colloidal suspension.[18]

As previously discussed, preventing interparticle plasmon coupling is critical to retain the individual enhancing performance of the NSts and, in turn, their full potential as powerful plasmonic substrates for quantitative applications. For instance, the yolk confined nanostars shown in Figure 5C enabled an outstanding single-particle quantitative response superior to their uncoated counterparts, with a dynamic range of concentration of benzenethiol (BT) that extends over 4 orders of magnitude (from ca. 10^{-5} to 10^{-10} M, Figure 6A).[13] Ultrasmall BT traces (i.e., $<10^{-10}$ M) can also be detected, but only qualitatively, since only one or zero molecules are present per NSts and SERS signals are observed only in clusters of yolk structures where the exact number of particles cannot be accurately determined.

Detection of the intrinsic SERS spectrum of a target analyte such as BT provides an example of an analytical application of SERS using a direct approach. While this sensing strategy is relatively straightforward for determining analytes with high affinity for the metallic surface, large Raman cross-section and dispersed in relatively simple media, it typically suffers from an important weaknesses when it needs to be applied under more conventional real-life scenarios which, thus, limit the viability of this strategy as an analytical tool.[83]

Conversely, indirect SERS approaches, where an extrinsic Raman reporter or a chemosensor is used to yield a SERS signal which is selectively and quantitatively correlated with the target recognition, have consistently shown superior qualities in terms of robustness, accuracy, multiplexity and selectivity, which makes them better suited for performing SERS analysis. In particular, the superior enhancing abilities of NSts in combination with advanced synthetic protocols for the finer tuning of their geometrical and chemical properties appoint these nanostructures as ideal candidates to be used as plasmonic enhancers in SERS-encoded nanoparticles (SEPs).[67a,80,82,84] This is particularly relevant for biomedical applications thanks to the tunability of the tip plasmonic resonances in the transparency biological window and the low cytotoxicity of gold nanoparticles.[84b,85] SEPs, or SERS tags, are typically used in place of fluorescent labels for indirect sensing. Differently from the fluorescent counterparts, SEPs combine high sensitivity and optical stability with theoretically unlimited multiplexing capabilities afforded by the unique vibrational fingerprints of RLs while quantitative information can be extracted as the overall SERS intensity can be engineered to scale linearly with the number of particles.[86] A representative example is a work performed by Jimenez de Aberasturi et al..[67a] Here, pegylated Au NSts were encoded with 5 different RLs and overcoated with the amphiphilic polymer polyisobutylene-alt-maleic anhydride (PMA) to impart high colloidal stability in biological media. To demonstrate their suitability for simultaneous multiplexing cell identification, five different breast cancer cell lines (HCC1395, SK-BR3, MDA.MB.231, CAMA1, and MCF-7) were separately incubated with each of the different SEPs and then combined into a single coculture. SERS mapping provided a quantitative analysis of the relative cell population

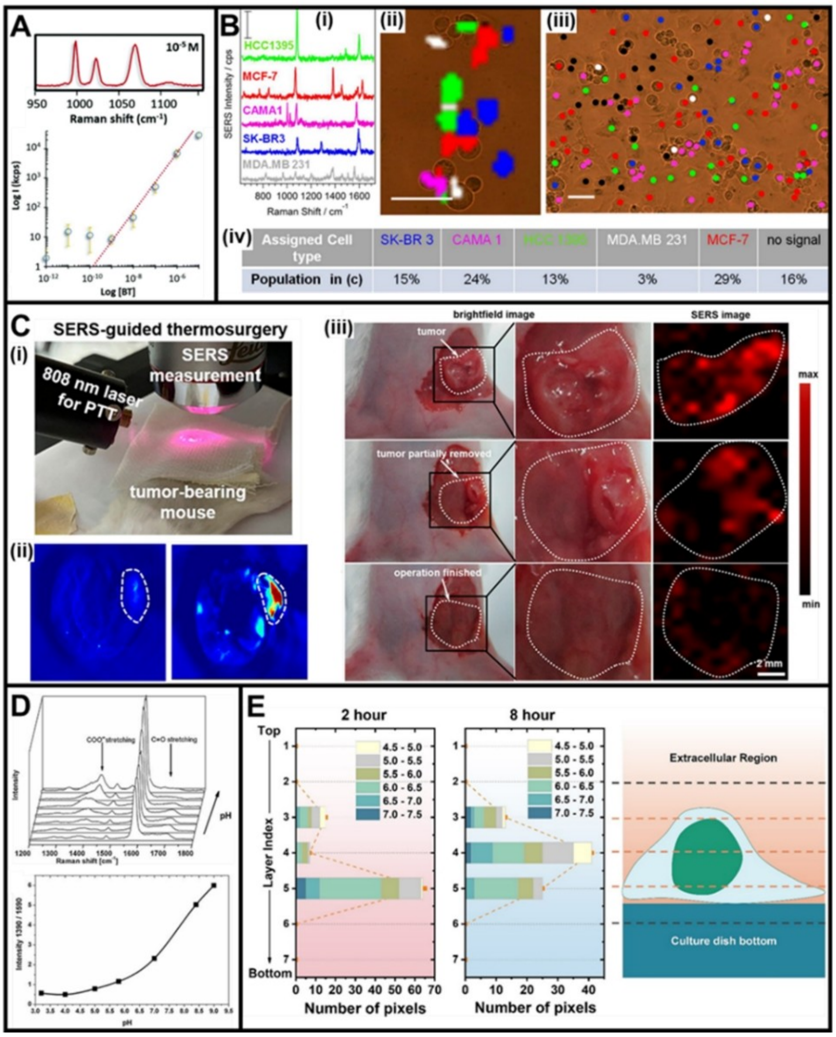

Assigned Cell type	SK-BR 3	CAMA 1	HCC 1395	MDA.MB 231	MCF-7	no signal
Population in (c)	15%	24%	13%	3%	29%	16%

Figure 6. (A) SERS spectra of benzenethiol (BT) recorded on AuNSt-mesoporous silica yolk-shell particles spin-coated on a silicon wafer after incubation with BT 10$^{<M->5}$M. SERS intensity as a function of BT concentration (logarithmic scales). Adapted with permission from ref. [13]. Copyright 2019, Royal Society of Chemistry. (B) (i) SERS spectra of 5 different silica-coated SERS-encoded AuNSt from single cell cultures (HCC1395, SK-BR3, MDA.MB.231, CAMA1, and MCF-7). (ii) Bioimaging with cell assignment. (iii, iv) Quantification of cellular composition via large-scale SERS single-point mapping of an area of 0.22 mm^2. Adapted with permission from ref. [67a]. Copyright 2016, American Chemical Society. (C) (i) Photograph of the experimental setup of the photoacoustic image-guided surgical resection of the primary tumor and intraoperative SERS detection of residual microtumors in a surgical bed. (ii) PA images of an orthotopic breast tumor-bearing mouse without (left) and with (right) the administration, via tail veil injection, of silica-coated SERS-encoded AuNst probes grafted with mPEG-silane (16 h after the injection). (iii) Real-time brightfield images and SERS images of PA image-guided surgical resection of tumor at three separate stages of the surgery: beginning, during and at the end (the white dotted line outlines the surgical bed of the primary tumor). Adapted with permission from ref. [80]. Copyright 2021, American Chemical Society. (D) SERS spectra of 4-MBA on BSA-stabilized silver nanoparticles aggregates in buffers at different pH. The characteristic pH dependence changes of the carboxylic stretching modes (COO and C=O) is also highlighted. In the bottom graph, it is displayed the pH calibration curve of the intensity ratio of the COO$^-$ and C=O bands as a function of pH. Adapted with permission from ref. [81]. Copyright 2010, Wiley-VCH. (E) pH range distribution extracted from internalized PA-coated 4-MBA-encoded AuNSt into a single live MCF7 cell at the different *x-y* planes (2 μm separation) as a function of pixel number with distinguishable SERS intensity of the 4-MBA band at 1081 cm^{-1}. Adapted with permission from ref. [82]. Copyright 2020, American Chemical Society.

within the coculture based on the unique spectral fingerprint of each RL (Figure 6B). In addition to be the most efficient single-particle SERS enhancers, AuNSts also display much higher extinction coefficient and large photothermal conversion efficiency than gold nanoparticles with different geometry.[72,80] On this basis, Wen et al.[80] exploited AuNSts to build a "three-in-one" theranostic nanoprobe for photoacoustic (PA) image-guided surgical resection of tumors and intraoperative SERS-guided thermosurgical elimination of residual microtumors (Figure 6C(i)) aimed at improving the surgical outcome by preventing tumor recurrence. AuNSts, encoded with a RL and coated with a silica layer, were further grafted with mPEG-silane to enhance both, biocompatibility and solubility. Nanoparticles were then administered via tail veil injection to an orthotopic breast tumor-bearing mouse. The well-known enhanced permeability and retention (EPR) effect allows for the preferential accumulation of the nanoprobes at the tumor sites in many animal models. PA imaging enables the identification of the main tumor margins, that are otherwise almost invisible in the tumor-bearing untreated mice

(Figure 6C(ii)), which is used as visual guidance to surgically resect the whole primary tumor. On the other hand, real-time SERS imaging precisely identifies residual tumor foci along the tumor-normal tissue boundary as well as satellite residual microtumors, aiding their removal via SERS-guided surgical resection (Figure 6C(iii)). Additionally, thermosurgery on the SERS-positive locations was carried out using a 5 minutes 808 nm-laser irradiation to selectively kill residual cancer cells by local plasmonic heating. The outer shell of nanostar-based SEPs can also be equipped with molecular elements (e.g., antibodies, aptamers) to impart active-tumor targeting abilities. For instance, Nicolson et al.[87] conjugated onto the silica shell encapsulating a SERS-encoded AuNSt a cyclic RGD peptide to selectively targeting glioblastoma multiforme (GBM) tumors *in vivo* in mice through the intact skull. This was achieved by implementing SERS imaging in the spatially offset modality (i.e., surface-enhanced spatially offset Raman spectroscopy, SESORS) which overcomes the intrinsic depth limitations of conventional Raman spectroscopy that inherently confine the SERS imaging to exposed tumors.[87]

It is also worth stressing that, when encoded with a chemoresponsive Raman molecule, AuNSts have also been exploited in the dynamic monitoring of biological processes at the cellular and subcellular level. A paradigmatic example is provided by the SERS imaging of the intracellular pH using 4-mercaptobenzonic acid (4-MBA) as a pH-sensitive molecule.[81–82,88] The degree of protonation of the carboxylic group of MBA produces spectral changes that can be quantitatively correlated with the pH value of the closest surroundings (Figure 6D). In a recent study, 4-MBA functionalized AuNSt were wrapped with an external layer of the cationic poly-l-arginine hydrochloride (PA) to grant high colloidal stability and cellular uptake together with a permeable layer that allows the free diffusion of protons to the 4-MBA modified gold surfaces.[82] Breast cancer cells (MCF7) were exposed to these nanoparticles and 3D SERS imaging of the intracellular pH was performed in living cells upon 2 and 8 hours before the initial incubation (Figure 6E). 3D imaging was carried out at 2 μm separated *x-y* planes along the orthogonal *z*-axis which localizes nanoparticles between levels 3 and 5, in agreement with the volumetric height of a live MCF7 cell (ca. 6–8 μm). Moreover, the pH values at different locations were also extracted from the analysis of the 4-MBA spectral profiles and compared, confirming that during the endocytosis route the nanomaterials move from pH 6–7 environments (endosomal compartment) to 4.5–5 pH subcellular compartments (mature lysosomes), similar to what has been observed with pH-sensitive fluorophores.[89] Another interesting work regarding the use of Au NSts for 3D cellular imaging exploits mechanical traps made of patterned nanoscale bilayers with four optically transparent arms that are coated with Au NSts. Such arms can be released to fold and wrap living cells, enabling the 3D molecular SERS profiling of the captured cell surfaces.[90] Additionally, new strategies for fast SERS imaging in 3D, such as SERS holography and widefield SERS microscopy are under development.[91]

Besides their use for *in vivo* applications, AuNSt-based SEPs have been integrated into an assortment of ex-vivo biosensors targeting a continuously broader range of different biomarkers and clinically relevant molecules[84c,92] adopting different sensing schemes. In this regard, an illustrative study has been performed by Villa et al.[84c] where they developed a SERS-based immunoassay for monitoring cortisol in biofluids (urine and serum). Cortisol is recognized as the main stress biomarker and high levels in biological fluids have been associated with serious health risks. The authors designed SEPs comprising AuNSts labelled with 4-MBA as RL and functionalized with HS-PEG-COOH and cortisol-BSA conjugates, which were integrated into two different immunoassay modalities: magnetically-assisted SERS immunoassay (MA-SERSI) and rigid substrate SERS immunoassay (RS-SERSI) (Figure 7A). In the first case, magnetic beads bearing cortisol antibodies were combined in suspension with SEPs, promoting the selective accumulation of the nanoparticles at the magnetic surfaces via antibody/cortisol-BSA binding. Upon addition of cortisol, SEPs are selectively displaced from the beads and, upon their magnetic separation from the media, the SERS intensity of the unbound 4-MBA labelled NSts is recorded in the supernatant. On the other hand, in the second modality, gold-coated glass slides decorated with the same cortisol antibodies similarly capture the SEPs at their surface. In this case, however, SERS measurements were performed on the dried solid substrates upon exposure to cortisol-containing fluids. Thus, while in the MA-SERSI scheme the SERS intensity linearly correlates with the cortisol content in the biofluids, in the RS-SERSI modality SERS signal decreases for increasing analyte concentrations (Figure 7A). It is worth noting that the RS-SERSI requires time-consuming washing steps and longer a-incubation times than the magnetic-based one. Limits of detection (LODs) were 7 ng/mL and 3 ng/mL for MA-SERSI and RS-SERSI, respectively (both well below the lower limit of normal cortisol levels in urine and serum), indicating a slightly better sensitivity for the second sensing modality. However, the MA-SERSI affords a better precision and a wider linear range of response which can be attributed to the experimental set-up that relies on the acquisition of a more reproducible SERS signal from individual SEPs freely moving within the scattering volume of the objective which avoids the conformational variability of the NSt adhesion onto gold-coated glass slides and the uncontrolled formation of nanoparticle clusters upon drying. Finally, MA-SERSI monitoring of cortisol in urine and serum was compared against two reference methods, Ultra Performance Liquid Chromatography-Mass Spectrometry (UPLC-MS) and Enzyme-Linked Immunosorbent Assay (ELISA), demonstrating major improvements in terms of sensitivity and repeatability, minimum sample preparation, simplicity, and portability.

In addition to SEPs, indirect SERS sensing approaches can also exploit SERS-active molecular receptors that selectively bind the target molecule undergoing structural changes that modify their electronic properties and/or conformational behaviour. These structural alterations produce spectral changes in the SERS spectra that are quantitatively correlated with the binding events. Among the wide variety of molecular

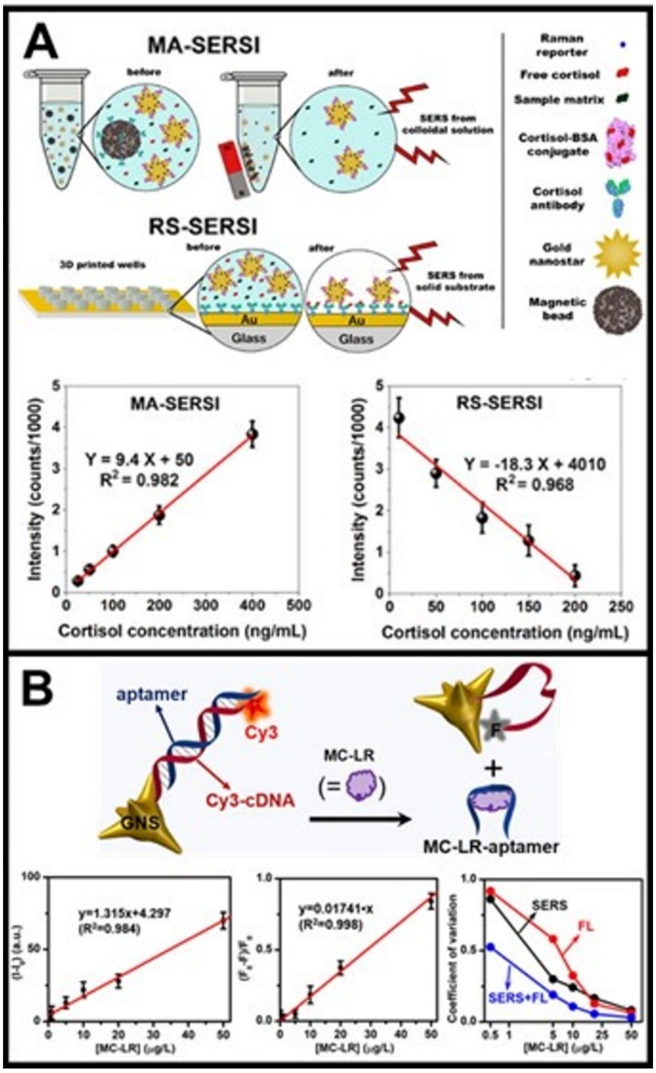

Figure 7. (A) Schematic of the two SERS-sensing modalities for the monitoring of cortisol content in biofluids using AuNSt-based encoded nanoparticles. MA-SERSI (magnetically assisted SERS immunoassay) employs a suspension of magnetic beads decorated with cortisol antibodies; the SERS intensity of the SEPs is measured in the supernatant. RS-SERSI (rigid substrate SERS immunoassay) adopts gold-coated glass decorated with cortisol antibodies; the SERS intensity of the SEPs is measured at the dried solid substrate. The corresponding calibration curves for cortisol quantification are also presented. Adapted with permission from ref. [84c]. Copyright 2020, Elsevier. (B) Outline of the fluorescence-SERS dual-modal aptasensor for detection of MC-LR in freshwaters (top). Calibration curves of the relative fluorescence intensity change ($(F_0{-}F)/F_0$) at 565 nm and SERS intensity at 1394 cm^{-1} ($I{-}I_0$) of the Cy3 dye vs. MC-LR concentration as well as the corresponding coefficients of variation (bottom). Adapted with permission from ref. [93]. Copyright 2020, American Chemical Society.

receptors reported in the literature, aptamers are one of the most exploited because of their high selectivity and reliable performances.[94] On the other hand, combining dual-mode optical sensing, such as SERS and fluorescence, into a single platform has been shown to improve the analytical merits of the detection such as precision and robustness, while eluding specific limitations of the single techniques.[93,95] For instance, Li et al.[93] employed gold nanostars to design a SERS-fluorescence aptamer-based biosensor (aptasensor) for sensitive and selective detection of hepatotoxin microcystin-LR (MC-LR) in freshwaters. A thiolated cyanine (Cy3) dye-modified complementary DNA (Cy3-cDNA) strand was attached to the surface of AuNSts via the formation of the strong Au–S bond and subsequently hybridized with the complementary aptamer to form a rigid Cy3-cDNA/aptamer duplex that forces the adoption of a tilted conformation with the Cy3 group spaced away from the metal surface (Figure 7B). In this scenario, Cy3 both SERS signal and fluorescence quenching are minimized (i.e., "SERS off" and "fluorescence on"), as the dye lays far from the plasmonic surface. In the presence of MC-LR, however, the aptamer is selectively captured to form the corresponding toxin/aptamer complex, enabling the Cy3-cDNA to freely bend and approximate the dye to the NSt surface which, in turn, causes an increase in SERS intensity and a drop of fluorescence emission (i.e., "SERS on" and "Fluorescence off"). The increase in SERS intensity ($I{-}I_0$) and the decrease in fluorescence emission ($(F_0{-}F)/F_0$) scale linearly with the toxin concentration in the 0.1 to 50 μg/L range. Notably, the dual-modal sensing yields a coefficient of variation, a statistical tool that shows the extent of data variability in a sample in relation to the mean of the population, which is lower than those of the individual optical measurements (Figure 7B), demonstrating the higher precision and accuracy of the dual-optical detection.

5. Conclusions

In recent years, much effort has been devoted to the development of NPs with the brightest SERS performance possible. NPs with intrinsic hotspots, such as NSts, were employed as SERS substrates because of their outstanding optical properties derived from the hotspots on the tips. Seedless approaches are fast and straightforward but usually have some inherent problems like producing undesired shapes in the solution and the difficulty of tuning the optical properties. On the other hand, the seed-mediated process allows precise control over the final product. However, although much progress has been made in controlling the homogeneity of NSts with an accessible surface to act as SERS substrates, more research is required to obtain a controllable, reproducible, and homogeneous synthesis. Availability of synthetic protocols for scalable nanomanufacturing of optically uniform gold nanostars with adjustable plasmonic response is key to directly translating the remarkable enhancing properties of these unique class of materials into commercially, and clinically, viable SERS applications. In particular, biocompatible star-shaped nanoparticles with tunable optical properties in the biological windows facilitate the implementation of SERS spectroscopy in biomedicine and, more prominently, in the areas of (ex-vivo and in-vivo) imaging and multiplex detection. This, combined with the new spectroscopic method such as SERS holography and widefield microscopy, which allows 3D imaging at an unprecedent speed, will for sure fuel the field for the generation of new sensing strategies for characterization and diagnosis.

Acknowledgements

This work is supported by the Ministerio de Ciencia Innovacion/AEI and the European Union Next Generation/PRTR (PID2020-120306RB-I00 and PDC2021-121787-I00), the AGAUR (2017SGR883), the Universitat Rovira i Virgili (2021PFR-URV-B2-02), the Cluster of Excellence 'Advanced Imaging of Matter' of the Deutsche Forschungsgemeinschaft (DFG) – EXC 2056 – project ID 390715994 and the ENSEMBLE3 project (GA No. MAB/2020/14) Foundation for Polish Science-European Union (GA.No. 857543).

Conflict of Interest

The authors declare no conflict of interest.

Keywords: nanocolloids · nanostars · sensing · SERS · surface plasmon resonance

[1] a) J. Langer, D. Jimenez de Aberasturi, J. Aizpurua, R. A. Alvarez-Puebla, B. Auguié, J. J. Baumberg, G. C. Bazan, S. E. J. Bell, A. Boisen, A. G. Brolo, J. Choo, D. Cialla-May, V. Deckert, L. Fabris, K. Faulds, F. J. García de Abajo, R. Goodacre, D. Graham, A. J. Haes, C. L. Haynes, C. Huck, T. Itoh, M. Käll, J. Kneipp, N. A. Kotov, H. Kuang, E. C. Le Ru, H. K. Lee, J.-F. Li, X. Y. Ling, S. A. Maier, T. Mayerhöfer, M. Moskovits, K. Murakoshi, J.-M. Nam, S. Nie, Y. Ozaki, I. Pastoriza-Santos, J. Perez-Juste, J. Popp, A. Pucci, S. Reich, B. Ren, G. C. Schatz, T. Shegai, S. Schlücker, L.-L. Tay, K. G. Thomas, Z.-Q. Tian, R. P. Van Duyne, T. Vo-Dinh, Y. Wang, K. A. Willets, C. Xu, H. Xu, Y. Xu, Y. S. Yamamoto, B. Zhao, L. M. Liz-Marzán, *ACS Nano* **2020**, *14*, 28–117; b) S. Schlücker, *Angew. Chem. Int. Ed.* **2014**, *53*, 4756–4795; *Angew. Chem.* **2014**, *126*, 4852–4894.

[2] J. Zhao, A. O. Pinchuk, J. M. McMahon, S. Li, L. K. Ausman, A. L. Atkinson, G. C. Schatz, *Acc. Chem. Res.* **2008**, *41*, 1710–1720.

[3] P. N. Njoki, I. I. S. Lim, D. Mott, H.-Y. Park, B. Khan, S. Mishra, R. Sujakumar, J. Luo, C.-J. Zhong, *J. Phys. Chem. C* **2007**, *111*, 14664–14669.

[4] R. Alvarez-Puebla, L. M. Liz-Marzán, F. J. García de Abajo, *J. Phys. Chem. Lett.* **2010**, *1*, 2428–2434.

[5] G. C. Phan-Quang, X. Han, C. S. L. Koh, H. Y. F. Sim, C. L. Lay, S. X. Leong, Y. H. Lee, N. Pazos-Perez, R. A. Alvarez-Puebla, X. Y. Ling, *Acc. Chem. Res.* **2019**, *52*, 1844–1854.

[6] R. Yu, L. M. Liz-Marzán, F. J. García de Abajo, *Chem. Soc. Rev.* **2017**, *46*, 6710–6724.

[7] V. Giannini, A. I. Fernández-Domínguez, S. C. Heck, S. A. Maier, *Chem. Rev.* **2011**, *111*, 3888–3912.

[8] P. Aldeanueva-Potel, E. Carbó-Argibay, N. Pazos-Pérez, S. Barbosa, I. Pastoriza-Santos, R. A. Alvarez-Puebla, L. M. Liz-Marzán, *ChemPhysChem* **2012**, *13*, 2561–2565.

[9] a) M. Liebtrau, M. Sivis, A. Feist, H. Lourenço-Martins, N. Pazos-Pérez, R. A. Alvarez-Puebla, F. J. G. de Abajo, A. Polman, C. Ropers, *Light-Sci. Appl.* **2021**, *10*, 82; b) M. Sivis, N. Pazos-Perez, R. Yu, R. Alvarez-Puebla, F. J. García de Abajo, C. Ropers, *Comm. Phys.* **2018**, *1*, 13.

[10] F. J. García de Abajo, A. Howie, *Phys. Rev. B* **2002**, *65*, 115418.

[11] U. Hohenester, A. Trügler, *Comp. Phys. Commun.* **2012**, *183*, 370–381.

[12] D. Barchiesi, T. Grosges, *J. Nanophoton.* **2014**, *8*, 083097.

[13] M. Blanco-Formoso, A. Sousa-Castillo, X. Xiao, A. Mariño-Lopez, M. Turino, N. Pazos-Perez, V. Giannini, M. A. Correa-Duarte, R. A. Alvarez-Puebla, *Nanoscale* **2019**, *11*, 21872–21879.

[14] V. Giannini, R. Rodríguez-Oliveros, J. A. Sánchez-Gil, *Plasmonics* **2010**, *5*, 99–104.

[15] a) N. C. Bigall, T. Härtling, M. Klose, P. Simon, L. M. Eng, A. Eychmüller, *Nano Lett.* **2008**, *8*, 4588–4592; b) A. Mehere, N. B. Chaure, *Appl. Phys. A* **2020**, *126*, 662; c) S. D. Perrault, W. C. W. Chan, *J. Am. Chem. Soc.* **2009**, *131*, 17042–17043.

[16] a) C.-H. Kuo, M. H. Huang, *Langmuir* **2005**, *21*, 2012–2016; b) H. Yuan, W. Ma, C. Chen, J. Zhao, J. Liu, H. Zhu, X. Gao, *Chem. Mater.* **2007**, *19*, 1592–1600.

[17] a) S. Atta, M. Beetz, L. Fabris, *Nanoscale* **2019**, *11*, 2946–2958; b) M. R. Langille, J. Zhang, M. L. Personick, S. Li, C. A. Mirkin, *Science* **2012**, *337*, 954.

[18] S. Barbosa, A. Agrawal, L. Rodríguez-Lorenzo, I. Pastoriza-Santos, R. A. Alvarez-Puebla, A. Kornowski, H. Weller, L. M. Liz-Marzán, *Langmuir* **2010**, *26*, 14943–14950.

[19] a) A. S. Barnard, N. P. Young, A. I. Kirkland, M. A. van Huis, H. Xu, *ACS Nano* **2009**, *3*, 1431–1436; b) J. L. Elechiguerra, J. Reyes-Gasga, M. J. Yacaman, *J. Mater. Chem.* **2006**, *16*, 3906–3919.

[20] P. Senthil Kumar, I. Pastoriza-Santos, B. Rodríguez-González, F. Javier García de Abajo, L. M. Liz-Marzán, *Nanotechnology* **2008**, *19*, 015606.

[21] C. G. Khoury, T. Vo-Dinh, *J. Phys. Chem. C* **2008**, *112*, 18849–18859.

[22] N. Pazos-Pérez, S. Barbosa, L. Rodríguez-Lorenzo, P. Aldeanueva-Potel, J. Pérez-Juste, I. Pastoriza-Santos, R. A. Alvarez-Puebla, L. M. Liz-Marzán, *J. Phys. Chem. Lett.* **2010**, *1*, 24–27.

[23] J. Cai, V. Raghavan, Y. J. Bai, M. H. Zhou, X. L. Liu, C. Y. Liao, P. Ma, L. Shi, P. Dockery, I. Keogh, H. M. Fan, M. Olivo, *J. Mater. Chem. B* **2015**, *3*, 7377–7385.

[24] A. S. De Silva Indrasekara, S. F. Johnson, R. A. Odion, T. Vo-Dinh, *ACS Omega* **2018**, *3*, 2202–2210.

[25] A. L. Siegel, G. A. Baker, *Nanoscale Adv.* **2021**, *3*, 3980–4004.

[26] H. Wang, Y. Pu, B. Shan, M. Li, *Inorg. Chem.* **2019**, *58*, 12457–12466.

[27] a) Y. Pu, Y. Zhao, P. Zheng, M. Li, *Inorg. Chem.* **2018**, *57*, 8599–8607; b) A. Kedia, P. S. Kumar, *J. Mater. Chem. C* **2013**, *1*, 4540–4549; c) A. Kedia, P. Senthil Kumar, *J. Phys. Chem. C* **2012**, *116*, 1679–1686.

[28] N. Ahmad, G. Wang, J. Nelayah, C. Ricolleau, D. Alloyeau, *Nano Lett.* **2017**, *17*, 4194–4201.

[29] W. Moukarzel, J. Fitremann, J.-D. Marty, *Nanoscale* **2011**, *3*, 3285–3290.

[30] J. Xie, J. Y. Lee, D. I. C. Wang, *Chem. Mater.* **2007**, *19*, 2823–2830.

[31] B. K. Jena, C. R. Raj, *Langmuir* **2007**, *23*, 4064–4070.

[32] a) X.-L. Liu, J.-H. Wang, S. Liang, D.-J. Yang, F. Nan, S.-J. Ding, L. Zhou, Z.-H. Hao, Q.-Q. Wang, *J. Phys. Chem. C* **2014**, *118*, 9659–9664; b) W. Xi, A. J. Haes, *J. Am. Chem. Soc.* **2019**, *141*, 4034–4042; c) G. Maiorano, L. Rizzello, M. A. Malvindi, S. S. Shankar, L. Martiradonna, A. Falqui, R. Cingolani, P. P. Pompa, *Nanoscale* **2011**, *3*, 2227–2232.

[33] D. H. Dam, J. H. Lee, P. N. Sisco, D. T. Co, M. Zhang, M. R. Wasielewski, T. W. Odom, *ACS Nano* **2012**, *6*, 3318–3326.

[34] a) R. M. Pallares, T. Stilson, P. Choo, J. Hu, T. W. Odom, *ACS Appl. Nano Mater.* **2019**, *2*, 5266–5271; b) G. Lu, T. Z. Forbes, A. J. Haes, *Analyst* **2016**, *141*, 5137–5143; c) K. Chandra, K. S. B. Culver, S. E. Werner, R. C. Lee, T. W. Odom, *Chem. Mater.* **2016**, *28*, 6763–6769.

[35] a) M. Gharib, M. Khalaf, S. Afroz, N. Feliu, W. J. Parak, I. Chakraborty, *ACS Sustainable Chem. Eng.* **2019**, *7*, 9834–9841; b) I. Chakraborty, W. J. Parak, *Adv. Mater. Interfaces* **2019**, *6*, 1801407.

[36] C. L. Nehl, H. Liao, J. H. Hafner, *Nano Lett.* **2006**, *6*, 683–688.

[37] S. Chen, Z. L. Wang, J. Ballato, S. H. Foulger, D. L. Carroll, *J. Am. Chem. Soc.* **2003**, *125*, 16186–16187.

[38] E. Nalbant Esenturk, A. R. Hight Walker, *J. Raman Spectrosc.* **2009**, *40*, 86–91.

[39] T. K. Sau, A. L. Rogach, M. Döblinger, J. Feldmann, *Small* **2011**, *7*, 2188–2194.

[40] F. Liebig, R. Henning, R. M. Sarhan, C. Prietzel, C. N. Z. Schmitt, M. Bargheer, J. Koetz, *RSC Adv.* **2019**, *9*, 23633–23641.

[41] P. Ndokoye, X. Li, Q. Zhao, T. Li, M. O. Tade, S. Liu, *J. Colloid Interface Sci.* **2016**, *462*, 341–350.

[42] A. Casu, E. Cabrini, A. Donà, A. Falqui, Y. Diaz-Fernandez, C. Milanese, A. Taglietti, P. Pallavicini, *Chem. Eur. J.* **2012**, *18*, 9381–9390.

[43] C. Morasso, D. Mehn, R. Vanna, M. Bedoni, E. Forvi, M. Colombo, D. Prosperi, F. Gramatica, *Mater. Chem. Phys.* **2014**, *143*, 1215–1221.

[44] a) A. Silvestri, V. Zambelli, A. M. Ferretti, D. Salerno, G. Bellani, L. Polito, *Contrast Media Mol. Imaging* **2016**, *11*, 405–414; b) M. Schütz, D. Steinigeweg, M. Salehi, K. Kömpe, S. Schlücker, *Chem. Commun.* **2011**, *47*, 4216–4218.

[45] J. Li, J. Wu, X. Zhang, Y. Liu, D. Zhou, H. Sun, H. Zhang, B. Yang, *J. Phys. Chem. C* **2011**, *115*, 3630–3637.

[46] L. Sun, J. Zhu, H. Zhang, B. Dou, W. Su, *Mater. Lett.* **2019**, *255*, 126502.

[47] a) S. V. Sheen Mers, S. Umadevi, V. Ganesh, *ChemPhysChem* **2017**, *18*, 1358–1369; b) S. Umadevi, H. C. Lee, V. Ganesh, X. Feng, T. Hegmann, *Liq. Cryst.* **2014**, *41*, 265–276; c) A. J. Blanch, M. Döblinger, J. Rodríguez-Fernández, *Small* **2015**, *11*, 4550–4559.

[48] G. Dacarro, P. Pallavicini, S. M. Bertani, G. Chirico, L. D'Alfonso, A. Falqui, N. Marchesi, A. Pascale, L. Sironi, A. Taglietti, E. Zuddas, *J. Colloid Interface Sci.* **2017**, *505*, 1055–1064.

[49] L.-C. Cheng, J.-H. Huang, H. M. Chen, T.-C. Lai, K.-Y. Yang, R.-S. Liu, M. Hsiao, C.-H. Chen, L.-J. Her, D. P. Tsai, *J. Mater. Chem.* **2012**, *22*, 2244–2253.

[50] B. Khlebtsov, E. Panfilova, V. Khanadeev, N. Khlebtsov, *J. Nanopart. Res.* **2014**, *16*, 2623.

[51] H. Yuan, C. G. Khoury, H. Hwang, C. M. Wilson, G. A. Grant, T. Vo-Dinh, *Nanotechnology* **2012**, *23*, 075102.

[52] H. Yuan, Y. Liu, A. M. Fales, Y. L. Li, J. Liu, T. Vo-Dinh, *Anal. Chem.* **2013**, *85*, 208–212.

[53] A. Silvestri, L. Lay, R. Psaro, L. Polito, C. Evangelisti, *Chem. Eur. J.* **2017**, *23*, 9732–9735.

[54] S. Abalde-Cela, P. Taladriz-Blanco, M. G. de Oliveira, C. Abell, *Sci. Rep.* **2018**, *8*, 2440.

[55] B. Andreiuk, F. Nicolson, L. M. Clark, S. R. Panikkanvalappil, Kenry, M. Rashidian, S. Harmsen, M. F. Kircher, *Nanotheranostics* **2022**, *6*, 10–30.

[56] J. Morla-Folch, L. Guerrini, N. Pazos-Perez, R. Arenal, R. A. Alvarez-Puebla, *ACS Photonics* **2014**, *1*, 1237–1244.

[57] W. Niu, Y. A. A. Chua, W. Zhang, H. Huang, X. Lu, *J. Am. Chem. Soc.* **2015**, *137*, 10460–10463.

[58] L. Zhang, X. Sha, Q. Fan, L. Han, Y. Yin, C. Gao, *Nanoscale* **2017**, *9*, 17037–17043.

[59] D. Zhu, Y. Liu, M. Liu, X. Liu, P. N. Prasad, M. T. Swihart, *J. Mater. Chem. B* **2020**, *8*, 5491–5499.

[60] N. Pazos-Perez, L. Guerrini, R. A. Alvarez-Puebla, *ACS Omega* **2018**, *3*, 17173–17179.

[61] J. Spadavecchia, S. Casale, J. Landoulsi, C.-M. Pradier, *Chem. Phys. Lett.* **2014**, *609*, 134–141.

[62] H.-L. Wu, C.-H. Chen, M. H. Huang, *Chem. Mater.* **2009**, *21*, 110–114.

[63] H.-G. Liao, Y.-X. Jiang, Z.-Y. Zhou, S.-P. Chen, S.-G. Sun, *Angew. Chem. Int. Ed.* **2008**, *47*, 9100–9103; *Angew. Chem.* **2008**, *120*, 9240–9243.

[64] P. Pallavicini, A. Donà, A. Casu, G. Chirico, M. Collini, G. Dacarro, A. Falqui, C. Milanese, L. Sironi, A. Taglietti, *Chem. Commun.* **2013**, *49*, 6265–6267.

[65] J. Zhu, M.-J. Liu, J.-J. Li, J.-W. Zhao, *Eur. Phys. J. B* **2017**, *90*, 216.

[66] L. Rodriguez-Lorenzo, R. A. Alvarez-Puebla, F. J. G. de Abajo, L. M. Liz-Marzan, *J. Phys. Chem. C* **2010**, *114*, 7336–7340.

[67] a) D. Jimenez de Aberasturi, A. B. Serrano-Montes, J. Langer, M. Henriksen-Lacey, W. J. Parak, L. M. Liz-Marzan, *Chem. Mater.* **2016**, *28*, 6779–6790; b) R. A. Álvarez-Puebla, R. Contreras-Cáceres, I. Pastoriza-Santos, J. Pérez-Juste, L. M. Liz-Marzán, *Angew. Chem. Int. Ed.* **2009**, *48*, 138–143; *Angew. Chem.* **2009**, *121*, 144–149.

[68] C. Fernández-López, C. Pérez-Balado, J. Pérez-Juste, I. Pastoriza-Santos, Á. R. de Lera, L. M. Liz-Marzán, *Soft Matter* **2012**, *8*, 4165–4170.

[69] M. Mueller, M. Tebbe, D. V. Andreeva, M. Karg, R. A. Alvarez Puebla, N. Pazos Perez, A. Fery, *Langmuir* **2012**, *28*, 9168–9173.

[70] W. Stöber, A. Fink, E. Bohn, *J. Colloid Interface Sci.* **1968**, *26*, 62–69.

[71] a) B. Mir-Simon, I. Reche-Perez, L. Guerrini, N. Pazos-Perez, R. A. Alvarez-Puebla, *Chem. Mater.* **2015**, *27*, 950–958; b) A. M. Fales, H. Yuan, T. Vo-Dinh, *Langmuir* **2011**, *27*, 12186–12190.

[72] C. Carrillo-Carrion, R. Martinez, M. F. Navarro Poupard, B. Pelaz, E. Polo, A. Arenas-Vivo, A. Olgiati, P. Taboada, M. G. Soliman, U. Catalan, S. Fernandez-Castillejo, R. Sola, W. J. Parak, P. Horcajada, R. A. Alvarez-Puebla, P. Del Pino, *Angew. Chem. Int. Ed.* **2019**, *58*, 7078–7082; *Angew. Chem.* **2019**, *131*, 7152–7156.

[73] X. R. Deng, S. Liang, X. C. Cai, S. S. Huang, Z. Y. Cheng, Y. S. Shi, M. L. Pang, P. A. Ma, J. Lin, *Nano Lett.* **2019**, *19*, 6772–6780.

[74] S. Atta, S. Rangan, L. Fabris, *ChemNanoMat* **2020**, *6*, 53–57.

[75] a) Y. Fu, M. Xin, J. Chong, R. Li, M. Huang, *J. Mater. Sci.* **2021**, *56*, 4151–4160; b) L. Zhang, C. Liu, Y. Gao, Z. Li, J. Xing, W. Ren, L. Zhang, A. Li, G. Lu, A. Wu, L. Zeng, *Adv. Healthcare Mater.* **2018**, *7*, 1801144.

[76] a) H. Fathima, L. Paul, S. Thirunavukkuarasu, K. G. Thomas, *ACS Appl. Nano Mater.* **2020**, *3*, 6376–6384; b) A. Mariño-Lopez, A. Sousa-Castillo, M. Blanco-Formoso, L. N. Furini, L. Rodríguez-Lorenzo, N. Pazos-Perez, L. Guerrini, M. Pérez-Lorenzo, M. A. Correa-Duarte, R. A. Alvarez-Puebla, *ChemNanoMat* **2019**, *5*, 46–50.

[77] A. Sousa-Castillo, L. N. Furini, B. D. B. Tiu, P.-F. Cao, B. Topçu, M. Comesaña-Hermo, B. Rodríguez-González, W. Baaziz, O. Ersen, R. C. Advincula, M. Pérez-Lorenzo, M. A. Correa-Duarte, *Adv. Mater.* **2018**, *30*, 1707598.

[78] S. Fornasaro, F. Alsamad, M. Baia, L. A. E. Batista de Carvalho, C. Beleites, H. J. Byrne, A. Chiadò, M. Chis, M. Chisanga, A. Daniel, J. Dybas, G. Eppe, G. Falgayrac, K. Faulds, H. Gebavi, F. Giorgis, R. Goodacre, D. Graham, P. La Manna, S. Laing, L. Litti, F. M. Lyng, K. Malek, C. Malherbe, M. P. M. Marques, M. Meneghetti, E. Mitri, V. Mohaček-Grošev, C. Morasso, H. Muhamadali, P. Musto, C. Novara, M. Pannico, G. Penel, O. Piot, T. Rindzevicius, E. A. Rusu, M. S. Schmidt, V. Sergo, G. D. Sockalingum, V. Untereiner, R. Vanna, E. Wiercigroch, A. Bonifacio, *Anal. Chem.* **2020**, *92*, 4053–4064.

[79] L. Rodriguez-Lorenzo, R. A. Alvarez-Puebla, I. Pastoriza-Santos, S. Mazzucco, O. Stephan, M. Kociak, L. M. Liz-Marzan, F. J. G. de Abajo, *J. Am. Chem. Soc.* **2009**, *131*, 4616–4618.

[80] Y. Wen, V. X. Truong, M. Li, *Nano Lett.* **2021**, *21*, 3066–3074.

[81] A. Pallaoro, G. B. Braun, N. O. Reich, M. Moskovits, *Small* **2010**, *6*, 618–622.

[82] Y. Z. Zhang, D. J. de Aberasturi, M. Henriksen-Lacey, J. Langer, L. M. Liz-Marzan, *ACS Sens.* **2020**, *5*, 3194–3206.

[83] L. Guerrini, R. A. Alvarez-Puebla, *Cancers* **2019**, *11*, 748.

[84] a) M. Bhamidipati, H. Y. Cho, K. B. Lee, L. Fabris, *Bioconjugate Chem.* **2018**, *29*, 2970–2981; b) L. Rodriguez-Lorenzo, Z. Krpetic, S. Barbosa, R. A. Alvarez-Puebla, L. M. Liz-Marzan, I. A. Prior, M. Brust, *Integr. Biol.* **2011**, *3*, 922–926; c) J. E. L. Villa, I. Garcia, D. J. de Aberasturi, V. Pavlov, M. Sotomayor, L. M. Liz-Marzan, *Biosens. Bioelectron.* **2020**, *165*.

[85] a) E. Lenzi, D. J. de Aberasturi, L. M. Liz-Marzan, *ACS Sens.* **2019**, *4*, 1126–1137; b) L. Rodriguez-Lorenzo, L. Fabris, R. A. Alvarez-Puebla, *Anal. Chim. Acta* **2012**, *745*, 10–23; c) Y. C. Ou, J. A. Webb, C. M. O'Brien, I. J. Pence, E. C. Lin, E. P. Paul, D. Cole, S. H. Ou, M. Lapierre-Landry, R. C. DeLapp, E. S. Lippmann, A. Mahadevan-Jansen, R. Bardhan, *Nanoscale* **2018**, *10*, 13092–13105.

[86] L. Guerrini, N. Pazos-Perez, E. Garcia-Rico, R. Alvarez-Puebla, *Cancer Nanotechn.* **2017**, *8*, 5.

[87] F. Nicolson, B. Andreiuk, C. Andreou, H. T. Hsu, S. Rudder, M. F. Kircher, *Theranostics* **2019**, *9*, 5899–5913.

[88] Y. Z. Zhang, I. Gallego, J. Plou, J. L. Pedraz, L. M. Liz-Marzan, J. Ciriza, I. Garcia, *Nanoscale* **2021**, *13*, 14354–14362.

[89] R. Hartmann, M. Weidenbach, M. Neubauer, A. Fery, W. J. Parak, *Angew. Chem. Int. Ed.* **2015**, *54*, 1365–1368; *Angew. Chem.* **2015**, *127*, 1382–1386.

[90] Q. Jin, M. Li, B. Polat, S. K. Paidi, A. Dai, A. Zhang, J. V. Pagaduan, I. Barman, D. H. Gracias, *Angew. Chem. Int. Ed.* **2017**, *56*, 3822–3826; *Angew. Chem.* **2017**, *129*, 3880–3884.

[91] a) M. Liebel, I. Calderon, N. Pazos-Perez, N. F. van Hulst, R. A. Alvarez-Puebla, *Angew. Chem. Int. Ed.* **2022**, https://doi.org/10.1002/anie.202200072; b) M. Liebel, N. Pazos-Perez, N. F. van Hulst, R. A. Alvarez-Puebla, *Nat. Nanotechnol.* **2020**, *15*, 1005–1011.

[92] a) Y. L. Wong, W. C. M. Kang, M. Reyes, J. W. P. Teo, J. C. Y. Kah, *ACS Infect. Dis.* **2020**, *6*, 947–953; b) J. X. Guo, Y. Liu, Y. L. Chen, J. Q. Li, H. X. Ju, *Chem. Sci.* **2018**, *9*, 5906–5911; c) S. Tanwar, V. Kaur, G. Kaur, T. Sen, *J. Phys. Chem. Lett.* **2021**, *12*, 8141–8150.

[93] M. Li, H. D. Lin, S. K. Paidi, N. Mesyngier, S. Preheim, I. Barman, *ACS Sens.* **2020**, *5*, 1419–1426.

[94] a) C. Catala, B. Mir-Simon, X. Feng, C. Cardozo, N. Pazos-Perez, E. Pazos, S. Gómez-de Pedro, L. Guerrini, A. Soriano, J. Vila, F. Marco, E. Garcia-Rico, R. A. Alvarez-Puebla, *Adv. Mater.* **2016**, *1*, 1600163; b) H. T. Ma, J. P. Liu, M. M. Ali, M. A. I. Mahmood, L. Labanieh, M. R. Lu, S. M. Iqbal, Q. Zhang, W. A. Zhao, Y. Wan, *Chem. Soc. Rev.* **2015**, *44*, 1240–1256.

[95] a) R. A. Alvarez-Puebla, N. Pazos-Perez, L. Guerrini, *Appl. Mater. Res.* **2018**, *13*, 1–14; b) J. Wang, R. Y. Zhang, X. T. Ji, P. P. Wang, C. F. Ding, *Anal. Chim. Acta* **2021**, *1141*, 206–213.

Manuscript received: February 9, 2022
Revised manuscript received: March 14, 2022
Accepted manuscript online: March 16, 2022
Version of record online: March 30, 2022